Resonance-Enhanced Multiphoton Ionization in the X-Ray Regime

Aaron C. LaForge[1,*] Sang-Kil Son (손상길)[2,3,†] Debadarshini Mishra[1] Markus Ilchen[4,5] Stephen Duncanson[1] Eemeli Eronen[6] Edwin Kukk[6] Stanislaw Wirok-Stoletow[2,7] Daria Kolbasova[2,7] Peter Walter[8] Rebecca Boll[4] Alberto De Fanis[4] Michael Meyer[4] Yevheniy Ovcharenko[4] Daniel E. Rivas[4] Philipp Schmidt[4] Sergey Usenko[4] Robin Santra[2,3,7] and Nora Berrah[1]

[1]*Department of Physics, University of Connecticut, Storrs, Connecticut 06269, USA*
[2]*Center for Free-Electron Laser Science CFEL, Deutsches Elektronen-Synchrotron DESY, 22607 Hamburg, Germany*
[3]*The Hamburg Centre for Ultrafast Imaging, 22761 Hamburg, Germany*
[4]*European XFEL, 22869 Schenefeld, Germany*
[5]*Institut für Physik und CINSaT, Universität Kassel, 34132 Kassel, Germany*
[6]*Department of Physics and Astronomy, University of Turku, 20014 Turku, Finland*
[7]*Department of Physics, Universität Hamburg, 22607 Hamburg, Germany*
[8]*Linac Coherent Light Source, SLAC National Accelerator Laboratory, Menlo Park, California 94025, USA*

Here, we report on the nonlinear ionization of argon atoms in the short wavelength regime using ultraintense x rays from the European XFEL. After sequential multiphoton ionization, high charge states are obtained. For photon energies that are insufficient to directly ionize a $1s$ electron, a different mechanism is required to obtain ionization to Ar^{17+}. We propose this occurs through a two-color process where the second harmonic of the FEL pulse resonantly excites the system via a $1s \rightarrow 2p$ transition followed by ionization by the fundamental FEL pulse, which is a type of x-ray resonance-enhanced multiphoton ionization (REMPI). This resonant phenomenon occurs not only for Ar^{16+}, but also through lower charge states, where multiple ionization competes with decay lifetimes, making x-ray REMPI distinctive from conventional REMPI. With the aid of state-of-the-art theoretical calculations, we explain the effects of x-ray REMPI on the relevant ion yields and spectral profile.

X-ray free-electron lasers (XFELs) [1,2] have offered new avenues for studying matter under intense femtosecond radiation. In this case, the system is highly excited or ionized during the XFEL pulse resulting in a multitude of new processes such as nuclear resonance superradiance [3], plasma dynamics in solids [4], and structural dynamics in complex molecular systems [5]. Simpler systems such as atoms [6–10], molecules [11–13], and clusters [14,15] provide a means to investigate multiphoton processes in a well-controlled manner. For longer wavelengths, multiphoton processes have been well studied. In particular, resonance-enhanced multiphoton ionization (REMPI) [16–18] has been a useful spectroscopic technique, since it provides a highly sensitive and selective means to ionize molecular compounds without strong fragmentation effects. As such, REMPI has been used in a wide variety of physical, chemical, and biological systems with recent applications in ultracold atom-molecule [19] and atom-atom [20] collisions, molecular chirality [21], catalytic surface chemistry [22], nuclear-spin conversion [23], and metrology [24,25].

REMPI relies on the laser wavelength being tuned to an electronic resonance, which leads to promotion to an excited state followed by ionization. As the absorption cross section for resonant excitation is typically stronger than the ionization cross section, REMPI provides an efficient means to ionize these systems at photon energies below the ionization threshold. Although XUV FELs have been used to show REMPI for shorter wavelengths [26,27], extending REMPI to the x-ray regime requires entirely different physical processes and interpretation. Conventional REMPI relies on the excitation of a valence electron where the only relaxation pathway is radiative decay. On the other hand, a core-excited electron after x-ray resonant excitation can additionally relax by Auger-Meitner [28] decay, which is orders of magnitude faster than radiative decay. Thus, the complex interplay between ultrafast decay processes and REMPI renders this fundamental nonlinear process challenging to fully resolve in the x-ray regime.

In this Letter, we observe nonlinear ionization to create Ar^{17+}, through a resonant two-color process in the x-ray regime. With the aid of state-of-the-art theoretical modeling, we attribute the ionization to a two-color REMPI-like process where the second harmonic of the FEL [29] creates a $1s \rightarrow 2p$ core excitation and the fundamental FEL pulse subsequently ionizes the system. The core excitation can occur for charge states up to Ar^{16+} where the lower charge
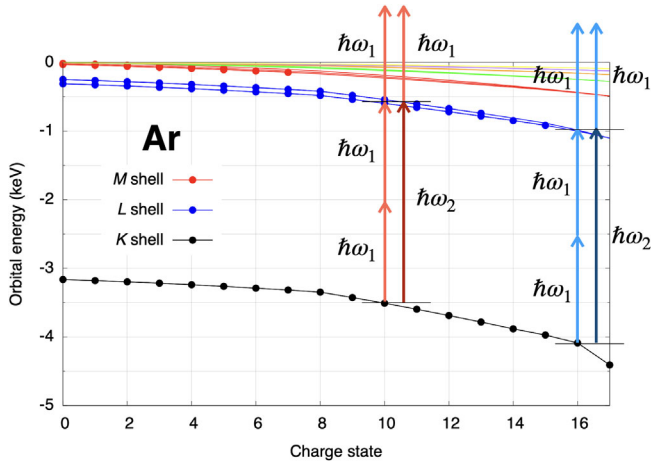
FIG. 1. Schematic of resonance-enhanced multiphoton ionization processes. The dark-colored arrows correspond to the second harmonic of the light-colored arrows, i.e., $\hbar\omega_2 = 2\hbar\omega_1$. The photon energies exemplified by the red arrows are smaller than the blue arrows. The orbital energies of the different electron shells are plotted as a function of the Ar charge state. See text for additional details.

states are influenced by their respective core-hole lifetimes. We find the observed broadband nature of the spectral resonance to be due to overlapping resonances with lower Ar charge states.

A schematic of the x-ray REMPI or XREMPI process is given in Fig. 1. For the higher charge states of Ar, the orbital energies shift to more negative values (higher binding energies). The relative shifts in energies between shells lead to new resonances occurring, dependent on the charge state and the photon energy. To illustrate this effect, we show the transitions for Ar^{10+} and Ar^{16+} with red and blue arrows, respectively, where the resonance shifts from ~3000 to ~3100 eV. To examine the formation of Ar^{17+}, let us first consider the transition $Ar^{16+} \rightarrow Ar^{17+}$, which has an ionization energy of 4130 eV [30]. For the case of an FEL photon energy of $\hbar\omega_1 = 1550$ eV, Ar^{16+} is produced through sequential multiphoton ionization [31], but Ar^{17+} cannot be produced through the absorption of another $\hbar\omega_1$ photon. Instead, resonant excitation can be achieved through either a direct $\hbar\omega_1$ two-photon process (excited to $1s2s$) or an $\hbar\omega_2$ one-photon process (excited to $1s2p$), where $\hbar\omega_2$ is the second harmonic of the FEL pulse ($\hbar\omega_2 = 2\hbar\omega_1$). These two processes are, respectively, represented by light and dark blue arrows in Fig. 1. Then, the resonantly excited states can be ionized by absorbing another $\hbar\omega_1$ photon. As such, the overall pathway occurs through either a one-color, three-photon $(2 + 1)$-REMPI or a two-color, two-photon $(1' + 1)$-REMPI, where the prime indicates the second harmonic.

Our experiment was performed using the Small Quantum Systems scientific instrument at the European XFEL [32,33]. In brief, soft x-ray FEL pulses with a nominal pulse length of 25 fs were focused to a size of approximately $1.5 \ \mu m \times 1.5 \ \mu m$ (FWHM) in the interaction region. The photon energy of the fundamental pulse was scanned from 1450 to 1583 eV with a measured energy bandwidth of approximately 1% (FWHM). The pulse energy varied from 2 to 6 mJ due to shot-by-shot fluctuations within the pulse train, which was measured upstream by an x-ray gas monitor detector [34]. From a previous measurement, the contribution of second harmonic radiation was estimated to be between 0.2 and 0.6% [35]. Because of the transmission of the grazing-incidence mirrors, third harmonic radiation is fully suppressed (4×10^{-9}) for the photon energies used in this experiment 36]]. The FEL beam crossed an effusive beam of Ar gas in the interaction region where an ion time-of-flight spectrometer was used to count ions on a shot-by-shot basis. To analyze and interpret our data, we performed theoretical calculations using XATOM [37–39], which solves coupled rate equations to simulate x-ray multiphoton multiple ionization dynamics with decay rates and cross sections calculated using the Hartree-Fock-Slater approach. To calculate direct two-photon and one-photon resonant absorption cross sections, we employed grid-based time-dependent configuration interaction singles [40,41] and an extended version of XATOM [42], respectively.

Figure 2 shows the ion yields of the high charge states $(> +10)$ of Ar as a function of the measured pulse energy for three cases: (a) below the resonance, (b) on the resonance, and (c) above the resonance. For completeness, the ion time-of-flight spectrum on the resonance is shown in Fig. 2(d) integrated over a measured pulse energy range of 4–6 mJ. The figure shows the higher charge states of Ar with Ar^{17+} and $^{36}Ar^{15+}$ shown in the inset. For Figs. 2(a)–2(c), the data are plotted on a log-log scale such that the slope of the distribution is proportional to the number of absorbed photons, as long as there is no saturation [31,43,44]. Overall, the ion yields show very similar power dependences for all three cases, with the exception of Ar^{17+}. For both above and below the resonance, the Ar^{17+} yield shows no dependence on the pulse energy. Given the statistical error, the yields fall within the experimental noise (gray area). On the other hand, when the photon energy is tuned to the resonance, the Ar^{17+} yield shows an increase for pulse energies greater than 4 mJ.

To further investigate this ionization process, we have measured the resonance spectral profile. Figure 3 presents the experimental yield ratio of Ar^{17+} to Ar^{16+} as a function of the photon energy at a pulse energy of 4.2 ± 0.1 mJ. The expected resonance positions, corresponding to half of the $1s2s(^1S_0)$ and $1s2p(^1P_1)$ transition energies of Ar^{16+} [45], are marked as solid vertical lines on the top of the figure. The $1s2s(^3S_1)$ state (dashed line) does not have a significant contribution to the resonance since the two-photon transition to this state is forbidden and the M1 one-photon transition is suppressed [46]. Nonetheless, our
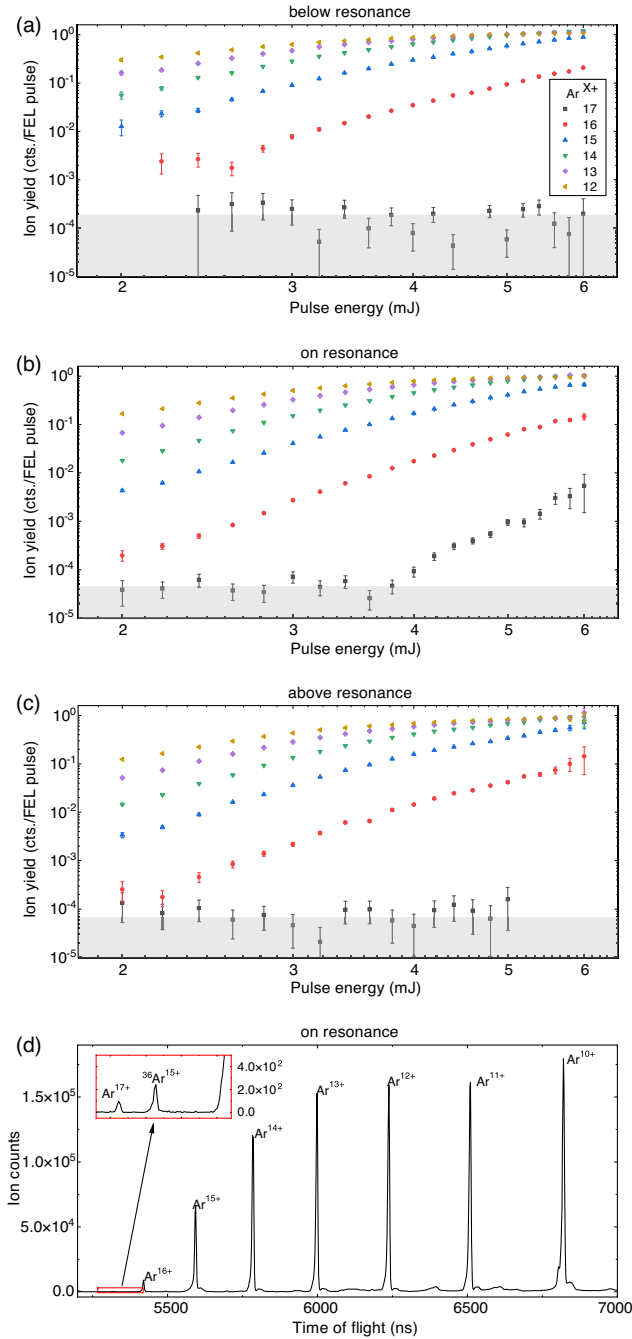
FIG. 2. Ion yields of Ar as a function of the measured FEL pulse energy for three cases: (a) Below the resonance, $\hbar\omega_1 = 1450$ eV; (b) on the resonance, $\hbar\omega_1 = 1550$ eV; and (c) above the resonance, $\hbar\omega_1 = 1576$ eV. The ion yields are given in counts per FEL pulse. The experimental noise for each measurement is given as a gray area. (d) Ion time-of-flight spectrum for $\hbar\omega_1 = 1550$ eV integrated over a measured pulse energy range of 4–6 mJ with the inset centered on Ar^{17+} and an isotope of Ar^{15+}.

FIG. 3. Ar^{17+} to Ar^{16+} yield ratio as a function of the photon energy at a pulse energy of 4.2 ± 0.1 mJ. Theoretical yield ratios for different pulse lengths with a fixed pulse energy of 4.2 mJ are given in different colors. The labels at the bottom indicate $1s \rightarrow 2p$ transitions for different charge states and electronic configurations. (a) Ar^{4+}: $1s^2 2s^2 2p^5 3p^5$. (b) Ar^{6+}: $1s^2 2s^2 2p^4 3p^4$, (c) Ar^{9+}: $1s^2 2s 2p^4 3s^2$, (d) Ar^{10+}: $1s^2 2s 2p^3 3s^2$, (e) Ar^{11+}: $1s^2 2s 2p^2 3s^2$, (f) Ar^{14+}: $1s^2 2p^2$, (g) Ar^{15+}: $1s^2 2p$, (h) Ar^{16+}: $1s^2$, and (i) Ar^{15+}: $1s^2 3p$. Here, the electron configurations are given before the transition. See text for additional details.

energies. These features are in stark contrast to the typical spectral dependence of REMPI at longer wavelengths, which gives sharp, narrow peaks when the laser is on the resonant transition. What causes these distinctions for XREMPI compared to conventional REMPI?

We first examine the pulse-length dependence of the resonance profile by using theoretical modeling in Fig. 3. The yield ratios are calculated for several pulse lengths, which are given as multiple colors. The dependence on other parameters is given in Figs. S1–S3 in the Supplemental Material [47]. Besides one-photon ionization by the fundamental pulse, one-photon ionization and resonant excitation by the second harmonic are included in the calculations for all charge states. We assume that the second harmonic contribution is 0.2% of the fundamental fluence and its bandwidth is equivalent to the fundamental bandwidth, which was measured to be ~1% for this experiment. On the other hand, direct two-photon excitation by the fundamental pulse is excluded since its contribution turns out to be negligible at fluences under consideration (see Fig. 4). The theoretical results are shifted on the x axis by the difference between one half of the $1s2p$ transition energy of Ar^{16+} calculated using XATOM (1551.3 eV) and the literature value (1569.8 eV) [45]. The results are volume integrated [39] with a pulse energy fixed at 4.2 mJ. Our calculations demonstrate that the peak position is shifted to lower photon energies and the profile width is broadened as the pulse length becomes shorter. Note that these effects on the resonance profile are not strongly sensitive to the calibrated peak fluence or

experimental data clearly show that (a) the peak position is redshifted compared to the literature values, and (b) the distribution is broad and asymmetric toward lower photon
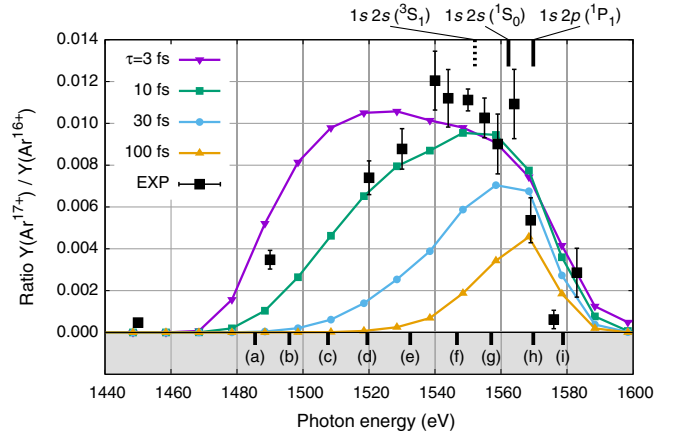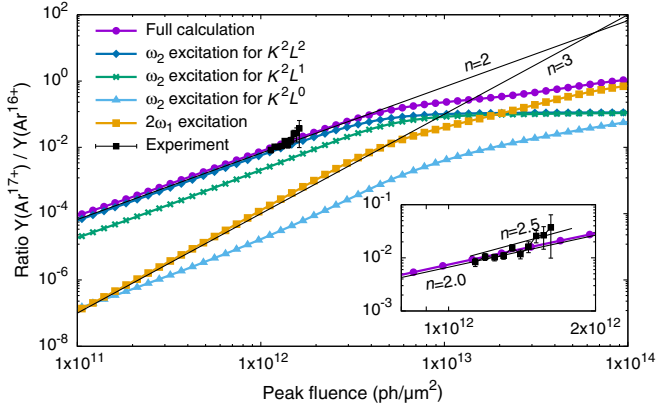
FIG. 4. Ar^{17+} to Ar^{16+} yield ratio as a function of the peak fluence at a photon energy of 1550 eV. Theoretical yield ratios are calculated including various contributions. See text for additional details. For the experimental data (black), the pulse energy is converted into the peak fluence based on a calibration using the ion yields of Ne [39]. Inset: Zoomed near the peak fluence of 1.6×10^{12} ph/μm^2 with fitted slopes.

transmission (see Fig. S1 in the Supplemental Material [47] for their resonance profile dependence). The calculated resonance profile with a pulse length of 10 fs fairly matches the experimental profile, which is consistent with a prior observation that the x-ray pulse length is a few times shorter than its nominal value [6].

For a conventional REMPI experiment using ultrashort laser pulses, the resonance profile is governed by the homogeneous bandwidth broadening due to the pulse length being shorter than the lifetime of the resonant state. In this case, the resonance profile can also be shifted due to the ac Stark effect since the intensity increases as the pulse length decreases, but the resonance peak still remains symmetric. Having said that, the measured resonance profile and its pulse-length dependence in Fig. 3 cannot be explained by conventional REMPI for the following reasons. First, the observed width (∼60 eV) is much broader than the FEL bandwidth, which corresponds to about 30 eV (∼1% of the second harmonic). In fact, for a self-amplified spontaneous emission (SASE) XFEL pulse, the bandwidth is not directly related to the pulse length but determined by the shortest pulse duration of the "spiky" pulses [48–52]. For our calculations, we employed the same FEL bandwidth for the various pulse lengths. Second, the observed redshift with respect to the resonances at Ar^{16+} is more than 10 eV, but the ac Stark shift in the x-ray regime is negligible (<0.2 eV) at the peak intensity under consideration (see Fig. S4 in the Supplemental Material [47]). Third, the resonance profile is asymmetric towards lower photon energies, which strongly hints that resonances occur for charge states lower than Ar^{16+}. When the pulse length becomes sufficiently long (∼100 fs), the resonance profile peaks at the resonance corresponding to the $1s2p$ transition of Ar^{16+} and its width is reduced to the FEL bandwidth of ∼30 eV.

To get a better insight into the XREMPI mechanism, we analyze the contributions of individual resonant processes occurring for all charge states including Ar^{16+}, at the peak of the resonance profile ($\hbar\omega = 1550$ eV) with a fixed pulse length of 10 fs. Figure 4 shows the ion yield ratios of Ar^{17+} to Ar^{16+} as a function of the calibrated peak fluence. Similar to Fig. 2, the experimental data are plotted on a log-log scale and fitted with a simple power function, $y = C \times x^n$, where n is a measure of number of photons absorbed. The fit yields a power dependence of $n = 2.5 \pm 0.6$, which points to a nonlinear ionization process by either three or two photons. We additionally plot theoretical ion yield ratios calculated for the various XREMPI pathways in Fig. 4. The purple (circles) curve represents the full XREMPI calculation including one-photon resonant excitation by the second harmonic (ω_2) and direct two-photon resonant excitation by the fundamental ($2\omega_1$), both of which are calculated for all charge states. For the ground state of Ar^{16+}, the direct two-photon cross section is explicitly calculated (see Fig. S5 in the Supplemental Material [47]). For the other charge states, we have assumed the same cross-section profiles, but shifted them according to the calculated transition energies. The orange (squares) curve indicates the calculated yield assuming only the direct two-photon resonant excitation cross sections, which results in a power dependence of three. The light blue (triangles) curve presents the calculation with the ω_2 excitation of $1s \rightarrow 2p$ only for electron configurations $K^2 L^0 M^m$, where $0 \leq m \leq 8$. The green (crosses) curve is for $K^2 L^1 M^m$, and the dark blue (diamonds) curve is for $K^2 L^2 M^m$.

Our analysis demonstrates that, even for the lower bound estimate of the second harmonic contribution (0.2%), the one-photon resonant excitation of $K^2 L^2 M^m$ by the second harmonic predominantly contributes to the formation of Ar^{17+} in the range of experimental peak fluences. Note that $K^2 L^2 M^m$ corresponds to the charge state of $+q$, where $+6 \leq q \leq +14$. In this case, a $1s$ vacancy is formed in the lower charge states, Ar^{q+}, and must survive until the final ionization step, i.e., Ar^{17+}. Thus, its ionization mechanism is characterized by $(1' + n)$-XREMPI from Ar^{q+} to Ar^{17+}, where $n = 17 - q$. This requires absorption of $(n + 1)$ photons and ejection of n electrons. On the other hand, formation of ground state Ar^{16+} from Ar^{q+} requires $(16 - q) = (n - 1)$ photons. Therefore, even for cases when $1s$ promotion occurs in the lower charge states, the Ar^{17+} to Ar^{16+} yield ratios plotted in Fig. 4 still yield a power dependence of two, except for the orange curve.

This $(1' + n)$-XREMPI process in the lower charge states can explain the asymmetric broadening of the resonance profile shown in Fig. 3 since the $1s \rightarrow 2p$ transition energy is shifted to smaller energies for the lower charge states, as shown in Fig. 1. Furthermore, ultrafast decay processes are critical in x-ray multiphoton ionization dynamics [31]. For example, the ion yields of Ar without decay processes are

substantially reduced (see Fig. S6 in the Supplemental Material [47]). If the pulse length is comparable to or shorter than the decay lifetimes, it is more likely that the $1s$ vacancy formed in the lower charge states can be further ionized before the decay process occurs (see Fig. S7 in the Supplemental Material [47] for Auger-Meitner and fluorescence lifetimes as a function of charge state). Surprisingly, the most probable XREMPI transition for a pulse length of 10 fs occurs for Ar^{14+}. In that case, the second harmonic first excites the $1s$ electron, followed by the absorption of three photons from the fundamental pulse in order to reach Ar^{17+}, which would be $(1' + 3)$-XREMPI. This way, the early-formed vacancy can survive over the course of sequential ionization up to $+17$, thus leaving its footprint on the resonance profile of Ar^{17+}/Ar^{16+}. This phenomenon resembles the quasinonsequential mechanism that is expected to lead to a breakdown of frustrated absorption [53,54]. Thus, the pulse-length sensitivity of the resonance profile is due to the various ionization pathways and associated decay lifetimes, rather than the bandwidth of the pulse.

It is worthwhile to compare XREMPI with resonance-enabled or enhanced x-ray multiple ionization (REXMI) [8,10], one of the distinctive phenomena in the field of XFEL-matter interactions. REXMI exploits a broad energy bandwidth to drive multiple resonant excitations for a range of charge states. After multielectron excitations, further ionization occurs via electron-correlation-driven relaxation processes. Because of the intrinsic broad bandwidth which characterizes SASE pulses [48–52], REXMI-type processes have been demonstrated as an ultra-efficient ionization mechanism in previous XFEL experiments. On the other hand, XREMPI involves a single-electron excitation, and further ionization occurs only by absorbing additional photons. Since XREMPI occurs only for a specific transition and charge state, it is beneficial to have a narrow bandwidth through the use of a monochromator or self-seeding techniques (see Fig. S8 in the Supplemental Material [47] for the resonance profiles calculated from narrower bandwidths).

In conclusion, we observed a novel type of REMPI in the x-ray regime experimentally and validated the process theoretically. Through sequential multiphoton ionization, neutral Ar is ionized to high charge states. For photon energies that are insufficient to directly ionize $1s$ electrons, promotion to Ar^{17+} requires a resonant process to create a $1s$ vacancy. We show that this occurs through a REMPI-like process where the second harmonic of the FEL promotes a $1s \rightarrow 2p$ transition and the fundamental FEL pulse subsequently ionizes the system further. That said, XREMPI is not restricted to a combination of the fundamental and second harmonic, and two-color capabilities at XFELs [55–57] could provide a desirable means to study XREMPI.

The resonance spectral profile of the XREMPI process shows a broad, asymmetric, redshifted distribution due to overlapping resonances with lower charge states, which is a clear distinction from conventional REMPI profiles at longer wavelengths. We have also demonstrated the strong dependence of the resonance profile on the pulse length, which is potentially applicable to characterize FEL beam parameters. With advances in seeding of XFELs and the availability of narrow bandwidth radiation [58,59], XREMPI can be used to reveal individual resonance structures in the spectral profile. This capability can be applied to perform precision spectroscopy on atoms or molecules; for example, highly charged ions of astrophysical relevance [60,61]. XREMPI also offers the powerful new aspect of element specificity in molecules, thereby opening up a novel spectroscopic technique to study x-ray ionization processes. For instance, with x rays, one can selectively excite one atom in a molecule and probe another atom. One can take advantage of the XREMPI technique to determine many physical processes such as charge migration from one site in the molecule to another position, thereby tracking the response of several different atoms in the molecule.

Data recorded for the experiment at the European XFEL are available on request at [62].

———

[*]aaron.laforge@uconn.edu
[†]sangkil.son@cfel.de

[1] C. Pellegrini, A. Marinelli, and S. Reiche, The physics of x-ray free-electron lasers, Rev. Mod. Phys. **88,** 015006 (2016).

[2] E. A. Seddon, J. A. Clarke, D. J. Dunning, C. Masciovecchio, C. J. Milne, F. Parmigiani, D. Rugg, J. C. H. Spence, N. R. Thompson, K. Ueda, S. M. Vinko, J. S. Wark, and W. Wurth,

Short-wavelength free-electron laser sources and science: A review, Rep. Prog. Phys. **80**, 115901 (2017).

[3] A. I. Chumakov, A. Q. R. Baron, I. Sergueev, C. Strohm, O. Leupold, Y. Shvyd'ko, G. V. Smirnov, R. Rüffer, Y. Inubushi, M. Yabashi, K. Tono, T. Kudo, and T. Ishikawa, Superradiance of an ensemble of nuclei excited by a free electron laser, Nat. Phys. **14**, 261 (2018).

[4] T. Kluge *et al.*, Observation of Ultrafast Solid-Density Plasma Dynamics using Femtosecond X-Ray Pulses from a Free-Electron Laser, Phys. Rev. X **8**, 031068 (2018).

[5] K. Nass *et al.*, Structural dynamics in proteins induced by and probed with x-ray free-electron laser pulses, Nat. Commun. **11**, 1814 (2020).

[6] L. Young *et al.*, Femtosecond electronic response of atoms to ultra-intense x-rays, Nature (London) **466**, 56 (2010).

[7] G. Doumy *et al.*, Nonlinear Atomic Response to Intense Ultrashort X Rays, Phys. Rev. Lett. **106**, 083002 (2011).

[8] B. Rudek, S.-K. Son, L. Foucar, S. W. Epp, B. Erk, R. Hartmann, M. Adolph, R. Andritschke, A. Aquila, N. Berrah *et al.*, Ultra-efficient ionization of heavy atoms by intense x-ray free-electron laser pulses, Nat. Photonics **6**, 858 (2012).

[9] H. Fukuzawa *et al.*, Deep Inner-Shell Multiphoton Ionization by Intense X-Ray Free-Electron Laser Pulses, Phys. Rev. Lett. **110**, 173005 (2013).

[10] B. Rudek *et al.*, Relativistic and resonant effects in the ionization of heavy atoms by ultra-intense hard x-rays, Nat. Commun. **9**, 4200 (2018).

[11] M. Hoener *et al.*, Ultraintense X-Ray Induced Ionization, Dissociation, and Frustrated Absorption in Molecular Nitrogen, Phys. Rev. Lett. **104**, 253002 (2010).

[12] J. P. Cryan *et al.*, Auger Electron Angular Distribution of Double Core-Hole States in the Molecular Reference Frame, Phys. Rev. Lett. **105**, 083004 (2010).

[13] A. Rudenko *et al.*, Femtosecond response of polyatomic molecules to ultra-intense hard x-rays, Nature (London) **546**, 129 (2017).

[14] H. Thomas *et al.*, Explosions of Xenon Clusters in Ultra-intense Femtosecond X-Ray Pulses from the LCLS Free Electron Laser, Phys. Rev. Lett. **108**, 133401 (2012).

[15] T. Gorkhover, M. Adolph, D. Rupp, S. Schorb, S. W. Epp, B. Erk, L. Foucar, R. Hartmann, N. Kimmel, K.-U. Kühnel, D. Rolles, B. Rudek, A. Rudenko, R. Andritschke, A. Aquila *et al.*, Nanoplasma Dynamics of Single Large Xenon Clusters Irradiated with Superintense X-Ray Pulses from the Linac Coherent Light Source Free-Electron Laser, Phys. Rev. Lett. **108**, 245005 (2012).

[16] P. Lambropoulos, Topics on multiphoton processes in atoms, in *Advances in Atomic and Molecular Physics*, edited by D. R. Bates and B. Bederson (Academic Press, New York, 1976), Vol. 12, pp. 87–164, https://dx.doi.org/10.1016/S0065-2199(08)60043-3.

[17] P. M. Johnson and C. E. Otis, Molecular multiphoton spectroscopy with ionization detection, Annu. Rev. Phys. Chem. **32**, 139 (1981).

[18] J. C. Miller and R. N. Compton, Fundamental studies of molecular multiphoton ionization, in *Second International Symposium on Resonance Ionization Spectroscopy and its Applications*, Conference Series Number 71, edited by G. S. Hurst and M. G. Payne (Institute of Physics, Bristol and Boston, 1984).

[19] N. Akerman, M. Karpov, Y. Segev, N. Bibelnik, J. Narevicius, and E. Narevicius, Trapping of Molecular Oxygen Together with Lithium Atoms, Phys. Rev. Lett. **119**, 073204 (2017).

[20] J. Wolf, M. Deiß, A. Krükow, E. Tiemann, B. P. Ruzic, Y. Wang, J. P. D'Incao, P. S. Julienne, and J. H. Denschlag, State-to-state chemistry for three-body recombination in an ultracold rubidium gas, Science **358**, 921 (2017).

[21] N. V. Vitanov and M. Drewsen, Highly Efficient Detection and Separation of Chiral Molecules Through Shortcuts to Adiabaticity, Phys. Rev. Lett. **122**, 173202 (2019).

[22] P. R. Shirhatti, I. Rahinov, K. Golibrzuch, J. Werdecker, J. Geweke, J. Altschäffel, S. Kumar, D. J. Auerbach, C. Bartels, and A. M. Wodtke, Observation of the adsorption and desorption of vibrationally excited molecules on a metal surface, Nat. Chem. **10**, 592 (2018).

[23] T. Sugimoto and K. Fukutani, Electric-field-induced nuclear-spin flips mediated by enhanced spin–orbit coupling, Nat. Phys. **7**, 307 (2011).

[24] M. Germann, X. Tong, and S. Willitsch, Observation of electric-dipole-forbidden infrared transitions in cold molecular ions, Nat. Phys. **10**, 820 (2014).

[25] M. Sinhal, Z. Meir, K. Najafian, G. Hegi, and S. Willitsch, Quantum-nondemolition state detection and spectroscopy of single trapped molecules, Science **367**, 1213 (2020).

[26] E. Shigemasa, M. Nagasono, H. Iwayama, J. R. Harries, and L. Ishikawa, Resonance-enhanced three-photon single ionization of Ne by ultrashort extreme-ultraviolet pulses, J. Phys. B **46**, 164020 (2013).

[27] G. M. Nikolopoulos and P. Lambropoulos, Resonantly enhanced multiphoton ionization under XUV FEL radiation: A case study of the role of harmonics, J. Phys. B **48**, 244006 (2015).

[28] D. Matsakis, A. Coster, B. Laster, and R. Sime, A renaming proposal: "The Auger–Meitner effect", Phys. Today **72**, No. 9, 10 (2019).

[29] G. Geloni, E. Saldin, E. Schneidmiller, and M. Yurkov, Exact solution for second harmonic generation in XFELs, Opt. Commun. **271**, 207 (2007).

[30] A. N. Artemyev, V. M. Shabaev, V. A. Yerokhin, G. Plunien, and G. Soff, QED calculation of the $n = 1$ and $n = 2$ energy levels in He-like ions, Phys. Rev. A **71**, 062104 (2005).

[31] R. Santra and L. Young, Interaction of intense x-ray beams with atoms, in *Synchrotron Light Sources and Free-Electron Lasers*, edited by E. Jaeschke, S. Khan, J. R. Schneider, and J. B. Hastings (Springer, Switzerland, 2016), pp. 1233–1260, https://dx.doi.org/10.1007/978-3-319-14394-1_25.

[32] T. Tschentscher, C. Bressler, J. Grünert, A. Madsen, A. P. Mancuso, M. Meyer, A. Scherz, H. Sinn, and U. Zastrau, Photon beam transport and scientific instruments at the European XFEL, Appl. Sci. **7**, 592 (2017).

[33] T. Mazza *et al.*, Mapping Resonance Structures in Transient Core-Ionized Atoms, Phys. Rev. X **10**, 041056 (2020).

[34] T. Maltezopoulos, F. Dietrich, W. Freund, U. F. Jastrow, A. Koch, J. Laksman, J. Liu, M. Planas, A. A. Sorokin, K. Tiedtke *et al.*, Operation of x-ray gas monitors at the European XFEL, J. Synchrotron Radiat. **26**, 1045 (2019).

[35] T. Tanaka, A. A. Sorokin, T. M. Baumann, K. Tiedtke *et al.* (to be published).

[36] T. Mazza *et al.* (to be published).

[37] S.-K. Son, L. Young, and R. Santra, Impact of hollow-atom formation on coherent x-ray scattering at high intensity, Phys. Rev. A **83**, 033402 (2011).

[38] Z. Jurek, S.-K. Son, B. Ziaja, and R. Santra, XMDYN and XATOM: Versatile simulation tools for quantitative modeling of x-ray free-electron laser induced dynamics of matter, J. Appl. Crystallogr. **49**, 1048 (2016).

[39] K. Toyota, Z. Jurek, S.-K. Son, H. Fukuzawa, K. Ueda, N. Berrah, B. Rudek, D. Rolles, A. Rudenko, and R. Santra, XCALIB: A focal spot calibrator for intense x-ray free-electron laser pulses based on the charge state distributions of light atoms, J. Synchrotron Radiat. **26**, 1017 (2019).

[40] A. Sytcheva, S. Pabst, S.-K. Son, and R. Santra, Enhanced nonlinear response of Ne^{8+} to intense ultrafast x rays, Phys. Rev. A **85**, 023414 (2012).

[41] S. Pabst and R. Santra, Time-dependent configuration interaction singles, in *Computational Strong-Field Quantum Dynamics*, De Gruyter Textbook Vol. 5, edited by D. Bauer (De Gruyter, Berlin and Boston, 2017), Chap. IV, pp. 169–201, https://dx.doi.org/10.1515/9783110417265-006.

[42] K. Toyota, S.-K. Son, and R. Santra, Interplay between relativistic energy corrections and resonant excitations in x-ray multiphoton ionization dynamics of Xe atoms, Phys. Rev. A **95**, 043412 (2017).

[43] M. G. Makris, P. Lambropoulos, and A. Mihelič, Theory of Multiphoton Multielectron Ionization of Xenon Under Strong 93-eV Radiation, Phys. Rev. Lett. **102**, 033002 (2009).

[44] M. Richter, S. V. Bobashev, A. A. Sorokin, and K. Tiedtke, Multiphoton ionization of atoms with soft x-ray pulses, J. Phys. B **43**, 194005 (2010).

[45] E. B. Saloman, Energy levels and observed spectral lines of ionized argon, Ar II through Ar XVIII, J. Phys. Chem. Ref. Data **39**, 033101 (2010).

[46] I. M. Savukov, W. R. Johnson, and U. I. Safronova, Multipole (E1, M1, E2, M2) transition wavelengths and rates between states with $n \leq 6$ in helium-like carbon, nitrogen, oxygen, neon, silicon, and argon, At. Data Nucl. Data Tables **85**, 83 (2003).

[47] See Supplemental Material at http://link.aps.org/supplemental/10.1103/PhysRevLett.127.213202 for additional theoretical figures and discussion, which includes Refs. [28,39,41,45].

[48] A. M. Kondratenko and E. L. Saldin, Generating of coherent radiation by a relativistic electron beam in an ondulator, Part. Accel. **10**, 207 (1980).

[49] R. Bonifacio, C. Pellegrini, and L. M. Narducci, Collective instabilities and high-gain regime in a free electron laser, Opt. Commun. **50**, 373 (1984).

[50] J. Andruszkow, B. Aune, V. Ayvazyan, N. Baboi, R. Bakker, V. Balakin, D. Barni, A. Bazhan, M. Bernard, A. Bosotti, J. C. Bourdon, W. Brefeld, R. Brinkmann, S. Buhler, J.-P. Carneiro *et al.*, First Observation of Self-Amplified Spontaneous Emission in a Free-Electron Laser at 109 nm Wavelength, Phys. Rev. Lett. **85**, 3825 (2000).

[51] S. V. Milton *et al.*, Exponential gain and saturation of a self-amplified spontaneous emission free-electron laser, Science **292**, 2037 (2001).

[52] N. Rohringer and R. Santra, X-ray nonlinear optical processes using a self-amplified spontaneous emission free-electron laser, Phys. Rev. A **76**, 033416 (2007).

[53] P. J. Ho, E. P. Kanter, and L. Young, Resonance-mediated atomic ionization dynamics induced by ultraintense x-ray pulses, Phys. Rev. A **92**, 063430 (2015).

[54] S.-K. Son, R. Boll, and R. Santra, Breakdown of frustrated absorption in x-ray sequential multiphoton ionization, Phys. Rev. Research **2**, 023053 (2020).

[55] T. Hara, Y. Inubushi, T. Katayama, T. Sato, H. Tanaka, T. Tanaka, T. Togashi, K. Togawa, K. Tono, M. Yabashi, and T. Ishikawa, Two-colour hard x-ray free-electron laser with wide tunability, Nat. Commun. **4**, 2919 (2013).

[56] A. A. Lutman, R. Coffee, Y. Ding, Z. Huang, J. Krzywinski, T. Maxwell, M. Messerschmidt, and H.-D. Nuhn, Experimental Demonstration of Femtosecond Two-Color X-Ray Free-Electron Lasers, Phys. Rev. Lett. **110**, 134801 (2013).

[57] S. Serkez *et al.*, Opportunities for two-color experiments in the soft x-ray regime at the European XFEL, Appl. Sci. **10**, 2728 (2020).

[58] J. Amann *et al.*, Demonstration of self-seeding in a hard-x-ray free-electron laser, Nat. Photonics **6**, 693 (2012).

[59] E. Hemsing, A. Halavanau, and Z. Zhang, Enhanced Self-Seeding with Ultrashort Electron Beams, Phys. Rev. Lett. **125**, 044801 (2020).

[60] S. Bernitt *et al.*, An unexpectedly low oscillator strength as the origin of the Fe XVII emission problem, Nature (London) **492**, 225 (2012).

[61] S. Kühn *et al.*, High Resolution Photoexcitation Measurements Exacerbate the Long-Standing Fe XVII Oscillator Strength Problem, Phys. Rev. Lett. **124**, 225001 (2020).

[62] The data supporting the findings of the presented study is available under https://doi.org/10.22003/XFEL.EU-DATA-002318-00.